Three dimensional sensitivity characterization of plasmonic nanorods for refractometric biosensors

V. Leitgeb,*[a] A. Trügler,[a] S. Köstler,[b] M. K. Krug,[a] U. Hohenester,[a] A. Hohenau,[a] A. Leitner[a] and J. R. Krenn[a]

An experimental three dimensional characterization of the local refractive index sensitivity of plasmonic gold nanorods is performed by controlled apposition of lithographic nanostructures. We show up to seven times higher sensitivity values to local changes in the refractive index at the particle tip than center. In addition, successive deposition of defined nm-thin dielectric layers on nanorods covered with stripe masks allows us to study the sensitivity decrease normal to the particle surface separately for different particle sites. Clear trends to a stronger sensitivity decay at sites of higher local sensitivity are demonstrated experimentally and theoretically. Our sensitivity characterization provides an important tool to find the most suitable particle type and particle site for specific bio-sensing applications.

Introduction

Plasmonic nanoparticles sustain collective oscillations of the conduction electrons, so-called localized surface plasmon resonances (LSPR), that are characterized by strong light absorption and scattering and a strong optical near field. The LSPR resonance frequency depends on the particle geometry, the dielectric function of the metal and the refractive index of the surrounding dielectric medium. Plasmonic particles enable the sensing of single nanoscale objects (*e.g.*, macromolecules) by transducing changes in the local refractive index into spectral plasmon resonance shifts, *i.e.*, wavelength shifts $\Delta\lambda_{LSPR}$.[1–6] Due to the rapid spatial decay of their optical near field into the surrounding medium, plasmonic particles outperform conventional devices based on propagating surface plasmon resonances (SPR) in sensing local and site-specific binding.[7,8]

In this work we experimentally and theoretically analyze the *local refractive index sensitivity* of rod-shaped plasmonic particles in three dimensions. The vast majority of previously published studies on refractometric sensing with particle plasmons has characterized the nanoparticle sensitivity in terms of bulk refractive index sensitivity, $S_{bulk} = \Delta\lambda_{LSPR}/\Delta n$, with n being the refractive index of the (assumed) bulk analyte medium surrounding the nanoparticle.[8] Sherry *et al.*[9] introduced a figure of merit defined as the peak shift per refractive index unit (RIU) divided by the LSPR full-width-at-half-maximum, to directly compare the overall performance of

single nanoparticles as refractometric sensors. In terms of bulk refractive index sensitivity, nanostructures of different shape but of the same material and resonance wavelength exhibit very similar sensing performance,[10] as the bulk sensitivity is averaged over sites of lower and higher sensitivity, given by the nanoparticle topology. However, in practical applications the bulk refractive index sensitivity is often a too coarse characterization of the nanoparticle sensing performance, as in most cases not the nanoparticle's optical response to changes in the bulk refractive index is of interest but the response to single (few) adsorbing macromolecules or nm-thin dielectric layers. A figure of merit for thin layers was introduced by J. Becker *et al.*[11] taking the sensing volume into account by considering the plasmon change induced by a small layer around the particle normalized to the layer thickness.

The spectral response of a metal nanoparticle to analyte access depends on the spatial overlap of its plasmonic near field and the analyte distribution.[12,13] As a consequence, the strongly inhomogeneous LSPR near field results in an inhomogeneous, *i.e.*, position dependent sensitivity. For example, in a previous work we have shown up to three times higher sensitivity values at the rim of a gold nanodisk than at its center.[14] In the following, we give a brief summary of the findings of other related research activities.

Unger *et al.*[15] examined the optical response of gold nanocrescents to the binding of a single dielectric colloid of 60 nm diameter by manipulating the position of the colloid relative to the nanocrescent's tip, showing that the nanoparticle response is intimately connected to the electromagnetic energy density at the binding site. Piliarik *et al.*[13] analyzed the sensitivity distribution of gold nanorods by applying polymer stripes to different positions of their surface, showing that the

[a] *Institute of Physics, University of Graz, Universitätsplatz 5, 8010 Graz, Austria.*
E-mail: verena.leitg@gmail.com
[b] *JOANNEUM RESEARCH Forschungsgesellschaft mbH, MATERIALS-Institut für Oberflächentechnologien und Photonik, Leonhardstraße 59, 8010 Graz, Austria*

nanoparticle sensitivity follows the profile of its electric field. Ament *et al.*[16] observed varying strong redshifts of the plasmonic resonance upon binding of single identical molecules to random positions along a gold nanorod. Zijlstra *et al.*[17] accomplished the plasmonic detection of single molecules in real time, reporting a broad distribution of spectral step sizes.

A theoretical model that helps to estimate the magnitude of a spectral shift upon analyte binding as a function of the chosen analyte and local field properties at the binding site was developed by Antosiewicz *et al.*[12] based on the electrostatic coupling theory of Davis *et al.*[18] Claudio *et al.*[19] used a stochastic diffusion-reaction simulation of biomolecular interactions on a plasmonic sensor surface, combined with calculations of the respective plasmon resonance peak shifts to quantify the relation between the number of bound molecules and the spectral response of the plasmonic sensor. They demonstrated that the shift in resonance wavelength of metal nanoparticles depends on the binding location of the dielectric analyte, as well as on geometrical and material particle parameters.

Murray *et al.*[10] characterized disk- and rod-shaped Au nanoparticles by coating them with nm thin Al_2O_3 layers, gaining better understanding of the particle's electric near field confinement. However, even in the case of nm-thin films the sensor signal is integrated over the whole particle area, allowing no spatially resolved sensitivity characterization.

By our three dimensional refractive index sensitivity characterization of plasmonic nanorods we provide an extensive experimental and theoretical characterization of nanoparticle sensing performance with regard to the particles' inhomogeneous sensitivity profile. We map the particle local sensitivity by placing nm-small dielectric dots to selected sites of the particle surface, mimicking the adhesion of large biomolecules. Additionally, we monitor the decay of the particle optical near field *spatially resolved* by deposition of defined nm-thin films to selectively covered particles. Up to seven times higher sensitivity values to local changes in the refractive index are found at the particles tips than at the particle center. We further observe a stronger decay of the nanorod sensitivity normal to the particle surface close to the particle tips.

Fabrication methods

Metal nanoparticles are fabricated by electron beam lithography using the positive resist poly(methyl methacrylate) (PMMA) on an indium–tin–oxide covered glass substrate. Following exposure, the PMMA layer is developed and gold is evaporated onto the resulting PMMA mask, followed by lift-off in acetone. We mainly concentrate on elongated particles, *i.e.*, nanorods, with dimensions of 110 ± 3 nm × 40 ± 3 nm, as measured in a scanning electron microscope (SEM). The nanorod height is 30 ± 0.5 nm, as measured with a calibrated quartz crystal thickness monitor. The nanorods are arranged in a square pattern with particle center-to-center distances of 200 nm in *x*-direction (long nanorod axis) and 100 nm in *y*-direction (short nanorod axis). The plasmon reso-
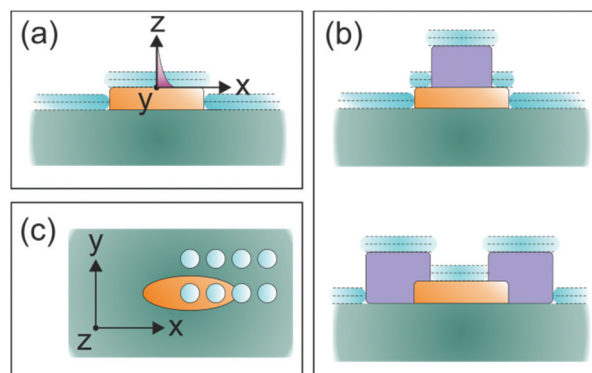
Fig. 1 Scheme of the characterization of the local refractive index sensitivity of plasmonic nanorods. Sketches of (a) a bare and (b) a PMMA stripe-mask (purple) covered nanorod, coated with SiO_2 layers (light blue). The sketch in (c) shows a nanorod with an attached SiO_2 dot (light blue) for eight exemplarily dot positions. Coordinate system as defined by the arrows, the plasmon field decay in *z*-direction is shown schematically in (a).

nance wavelengths of the arrays when exposed to air are 733 nm (long rod axis) and 535 nm (short rod axis).

A first characterization of the particle sensitivity profile in *z*-direction, *i.e.*, normal to the particle surface, is obtained by successive evaporation of defined nm-thin SiO_2 layers on top of nanoparticles and layer-by-layer nanocoating by consecutive polyelectrolyte adsorption, see Fig. 1(a). The optical response of gold nanorods to the SiO_2 multilayers is compared to gold nanodisks (160 ± 3 nm diameter, 30 ± 0.5 nm height) as characterized in our previous work.[14] The fabrications procedure of the disk-shaped particles follows the one for nanorods.

The *three dimensional characterization* of the nanorod sensitivity is performed by controlled apposition of lithographic nanostructures. To retrieve laterally resolved sensitivity information in *z*-direction we cover specific areas of nanorods with PMMA stripes (60 nm high) in a second electron beam lithography step immediately after nanorod fabrication. These surface-masks restrict the following layer deposition to selected particle sites, see Fig. 1(b), enabling a localized characterization of the sensitivity profile. The alignment of the stripe-masks with the nanorods is achieved with an accuracy of ±5 nm using a set of lithographed alignment marks.

The particle sensitivity profile in *x*- and *y*-direction is obtained by the lithographically controlled apposition of SiO_2 dots (20 ± 3 nm diameter, 20 ± 0.5 nm height) to selected positions on and around the nanoparticle surface, see Fig. 1(c). As the SiO_2 dots are of similar dimensions as very large biomacromolecules they represent a suitable model for specific nanoparticle–biomolecule interactions. The volume ratio of SiO_2 dot/gold nanorod is approximately 0.05.

Simulation methods

The local sensitivity measurements are supported by simulations with the MNPBEM toolbox.[20] This simulation package

is based on the boundary element method[21] and solves Maxwell's equations for arbitrary particle shapes. The nanorods (110 nm × 40 nm, height 30 nm) are modelled according to the experimental values. The dielectric function for gold is adopted from tabulated data,[22] the refractive index of the SiO_2 dot is $n = 1.5$. The substrate supporting the gold nanorods is included in the simulations. The number of surface elements of the discretized nanorod and dot structure is increased until convergence is reached, in the immediate vicinity of the dielectric dot the surface mesh of the nanorod is particularly refined.

Results and discussion

Sensitivity characterization in *z*-direction

The optical responses of an array of bare nanorods and an array of bare nanodisks to an increasing number of SiO_2 multi-layers are shown in Fig. 2. The nanoparticle arrays are measured in transmission mode with a standard optical microscope (Zeiss, Axioskop 2) combined with a photodiode array spectrometer (Zeiss, MMS-1), under white light illumination polarized along the long nanorod axis (*x*-direction). For the evaluation of the LSPR spectral shift we employ an algorithm tracking the centroid (center of mass) of the optical spectra.[23] The change in centroid position upon adding a given dielectric layer or nanostructure is a direct measure of the nanoparticle sensitivity. Changes in centroid position and changes in the actual peak of the spectrum are linearly related with a proportionality constant always close to 1.[23] We note that systematic studies of the reproducibility of environmental induced centroid shifts showed deviations in shift strength of <10% for different arrays of the same particle type.

The measurement setup can in principle yield a peak position precision of <0.001 nm. However, sample-removal for SiO_2 evaporation and reinstallation before each measurement step

introduces uncontrollable minor variations in the nanorod array position with respect to the spectrometer slit that limits the peak position precision to approximately ±0.5 nm.

When covering nanoparticles completely with SiO_2 (thickness 60 nm) we observe a bulk sensitivity of 167 nm RIU^{-1} and 112 nm RIU^{-1} for the array of nanorods and the array of nanodisks, respectively. We note that by choosing the above mentioned particle geometries the initial spectral position of the respective LSPRs are almost identical, 733 nm for nanorods and 738 nm for nanodisks.

The deposition of the first SiO_2 layer (thickness 3.5 nm) causes a 1.5 times stronger centroid shift for nanorods than for nanodisks. The spectral shifts induced by further additional layers show that the sensitivity (*i.e.*, relative centroid shift) in *z*-direction decreases stronger for the nanorods than for the nanodisks. We fit the data assuming single exponential decay[24,25] which, although being obviously an oversimplification for a three-dimensional nanostructure, is in good accordance with the experimental values. We yield decay length values of 16 nm for the nanorod and 21 nm for the nanodisk (Fig. 2(a)) with a standard error of ±1 nm. This is indicative of a higher sensitivity to changes in local (*i.e.*, close to their surface) refractive index due to a more confined plasmonic field for nanorods in comparison to nanodisks of the same initial LSPR wavelength. We note that the presence of the substrate supporting the nanoparticles might affect the distribution of their plasmonic near field in a way that slightly enhances differences in field confinement between disk- and rod-shaped particles, *cf.* Murray *et al.*[10] In the following we concentrate on the higher sensitive rod-shaped nanoparticles.

A spatially resolved study of the nanorod refractive index sensitivity profile in *z*-direction is possible by applying PMMA stripe masks to the particles. Two types of masks, denoted as center and tip masks, cover either the central area of each nanorod or the outmost particle tips, as well as the area in
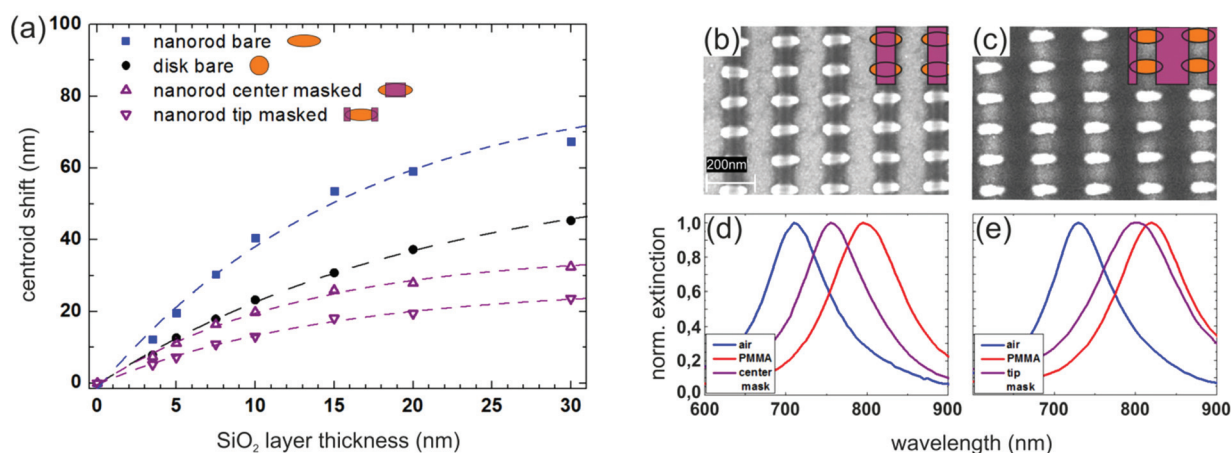
Fig. 2 (a) Nanorod LSPR centroid shifts *vs.* SiO_2 layer thickness for an array of bare nanorods (full blue squares), bare nanodisks (full black circles), center masked nanorods (purple triangles, tip up) and tip masked nanorods (purple triangles, tip down). The error is within the size of the symbols. The dashed lines are single exponential fits to the data points. Right panels: (b) SEM images of gold nanorods masked with 60 nm high PMMA stripes at the particle center and (c) tip and sketches of the particle and mask geometries. The lower panels show normalized extinction spectra of nanorod arrays with the rods being bare (blue lines), stripe-masked (purple lines, (d) center and (e) tip masked) and fully PMMA covered (red lines).

between two nanorods, see Fig. 2(b) and (c), respectively. The center masks leave up to about 20 nm of the particle tip uncovered, while the tip masks leave the nanorod centers uncovered up to off-center distances (*i.e.*, distances from the center of the nanorod in *x*-direction, see Fig. 1) of about 30 nm. Fig. 2(d) and (e) show extinction spectra of exemplary gold nanorod arrays utilized in the sensitivity characterization with the nanorods being bare, PMMA masked and fully PMMA covered. When covering the particles completely with PMMA we observe a redshift of 83 ± 0.5 nm, with PMMA having a refractive index of 1.49 at a wavelength of 700 nm. Applying the center mask (Fig. 2(d)) redshifts the nanorod LSPR wavelength by 45 ± 0.5 nm, the tip mask (Fig. 2(e)) leads to a shift of 57 ± 0.5 nm.

The redshifts in centroid wavelength caused by the successively evaporated thin SiO_2 layers on top of a center and a tip masked nanoparticle array are plotted in Fig. 2(a) (purple symbols). The first SiO_2 layer, with a thickness of 3.5 nm, shifts the centroid of the center masked particles (free tips, Fig. 2(b)) about 1.4 times stronger than for tip masked nanorods (free center, Fig. 2(c)). Assuming again single exponential decay in sensitivity with increasing surface distance (and thus layer number), the center masked nanorod sensitivity decreases to its $1/e$ value at a surface distance of 13 ± 1 nm, the corresponding value for the tip masked nanorod is 14 ± 1 nm.

SiO_2 layers give a first indication of the optical response and thus sensitivity of nanoparticles upon deposition or binding of organic thin-films. To probe the particle refractive index sensitivity profile in *z*-direction more realistically we chose layer-by-layer deposition of nm-thick polyelectrolyte (PE) multilayers, mimicking biological thin-films. PE layers form homogeneous layers and are widely used to create functional multilayered surface coatings.[26] For the PE multilayer assembly we incorporate the substrate supporting the nanorod array into a flow-cell that allows introducing and changing the liquid environment, *i.e.*, polyelectrolyte and buffer solutions. Nanoparticle arrays are measured in transmission mode as described above, with a spectral position precision of the measurement setup of <0.001 nm. As a first PE layer we apply polyethylenimine (PEI), then alternately poly-4-styrenesulfonate Na-salt (PSS) and polyallylamine hydrochloride (PAH). The PEs are consecutively applied at a concentration of 20 mM in 0.5 M KCl for 10 min followed by rinsing with 0.5 M KCl solution. Using PEI as the first layer prohibits insular deposition of the subsequent PSS and PAH layers and promotes a homogeneous and linear layer-by-layer growth.[26,27]

The thickness of a PSS/PAH bilayer is determined by means of a quartz crystal micro balance with dissipation monitoring (QCM-D) in a separate experiment. See Fig. 3. In aqueous media the acoustic waves penetrate to a depth around 250 nm from the surface[28] and hence allow to measure the thickness of the whole multilayer coating. An E-4 QCM-D device from Q-Sense AB (Gothenburg, Sweden) is used for quartz microgravimetry experiments, using gold covered quartz crystal resonators with a resonance frequency of 4.95 MHz. The crystals are
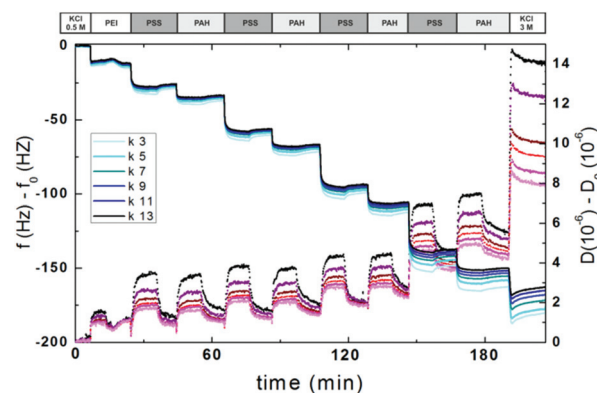

Fig. 3 Real-time frequency (bluish graphs) and dissipation (reddish graphs) responses of the QCM-D biosensors to PE layer adsorption for different overtone numbers *k*. The signals obtained while incubating with the KCl buffer are considered as $f_0 = 0$ and $D_0 = 0$.

cleaned in ammonium peroxide solution (NH_3 (25%) : H_2O_2 (30%) : deionized water = 1 : 1 : 5) solution at 75 °C for 10 min, thoroughly rinsed with deionized water and subsequently cleaned by O_2 plasma treatment for 2 min using a Diener Femto Plasma System. Polyelectrolyte adsorption experiments are carried out by rinsing the measurement chamber with the respective polyelectrolyte and buffer solutions at a flow rate of 0.1 ml min^{-1} and continuously recording resonance frequency shift and dissipation values.

Adsorbed areal masses are calculated from the shifts in resonance frequency using the Sauerbrey equation[29] $\Delta m = C\Delta f/k$, where Δf is the resonance frequency shift, $C = 17.7$ ng cm^{-2} Hz (at $f = 5$ MHz) is the mass sensitivity constant and k (= 1,3,5,...) is the overtone number (all frequency shifts reported in this manuscript are already divided by the respective overtone number). Polyelectrolyte layer thicknesses are calculated from the areal mass determined by the QCM-D according to Iturri Ramos *et al.*[30] The frequency shift per layer is *ca.* 10 Hz for PAH and *ca.* 23–25 Hz for PSS, corresponding to areal masses of roughly 200 ng cm^{-2} (PAH) and 410–450 ng cm^{-2} (PSS), or layer thicknesses of 1.7–2 nm (PAH) and *ca.* 4 nm (PSS). For the first PEI layer slightly more than 200 ng cm^{-2} are obtained, corresponding to a thickness of approximately 2 nm. Similar results for the PEI layer are determined on bare gold nanorods from LSPR transmission spectra. On center masked particles, however, we observe layer heights of only about half a nanometer. We attribute this to PEI macromolecules binding not only to the gold particles but due to the high PMMA electronegativity also to the PMMA mask. We therefore restrain from PE measurements on tip masked nanorods as here the PMMA mask is quite large in comparison to the uncovered gold surface.
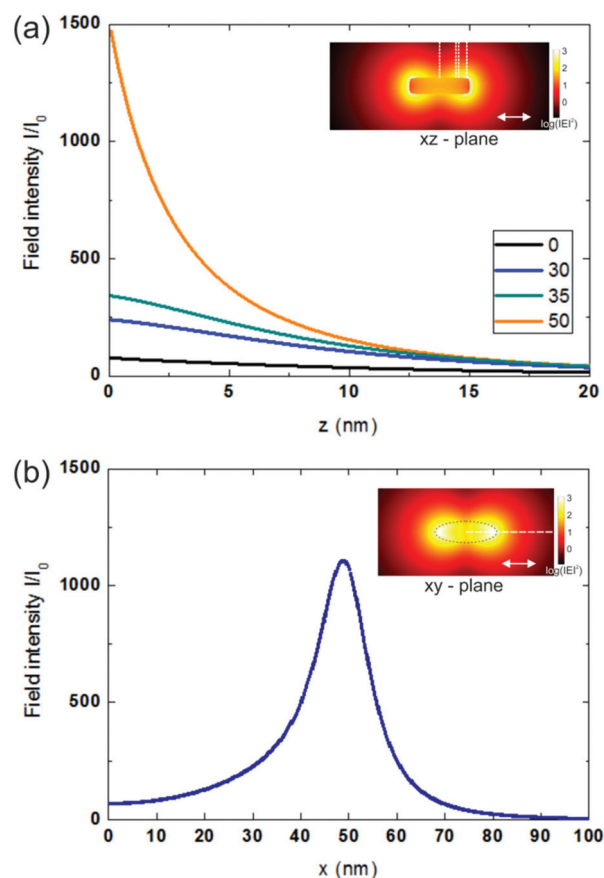
The centroid wavelength of a nanorod array upon successive deposition of PE layers is plotted in Fig. 4(a), showing a step-growth that decreases in centroid shift with increasing layer number. Fig. 4(b) shows the centroid shifts of a bare and a center masked nanoparticle array plotted against PE layer thickness. The decrease in centroid shift for higher layers is
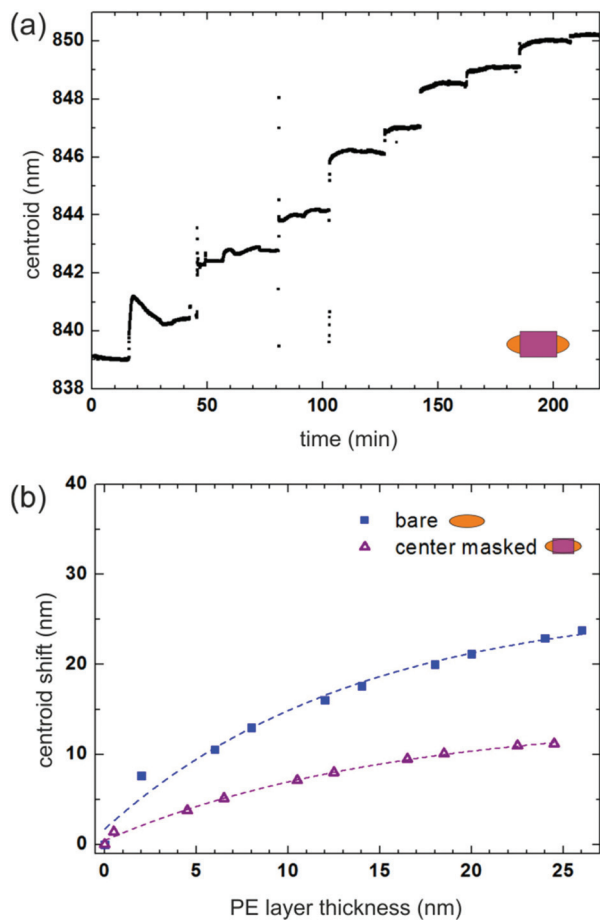
Fig. 4 PE layers on gold nanorods. (a) Exemplary centroid wavelength shift of a center masked nanorod array immersed in buffer solution upon successive adhesion of PE layers. The discontinuities at minute 46, 81 and 103 are caused by air bubbles passing through the measuring chamber. (b) Centroid shifts of a bare and a center masked nanorod array plotted against the thickness of the PE multilayer. The error is within the size of the symbols. The dashed lines are single exponential fits to the measured data points.

Fig. 5 Simulated field intensities of gold nanorods ($110 \times 40 \times 30$ nm^3). Panel (a) shows the electric near field profile in the xz-plane for off-center distances x as given in the legend ($y = 0$). The same is plotted in panel (b), but for the xy-plane at the upper particle surface at $z = 1$ nm. The insets of (a) and (b) show the logarithmically plotted simulated field intensities of a nanorod in side and top view, respectively, the white lines depict the positions of the shown electric near field profiles. The double arrows indicate the polarization direction.

again attributed to the diminished sensitivity at larger distances perpendicular to the nanorod surface, since PE multilayers comprised of PSS and PAH display linear growth under the chosen adsorption conditions.[26] As in Fig. 3 a sequence of consecutive stronger and weaker centroid shifts for PSS and PAH layers due to their different thicknesses can be seen.

Covering the bare nanorod array with a 50 nm thick PE layer (not shown) shifts its centroid wavelength for about 29 nm. With the difference in refractive index between the buffer solution and PE being 0.17 RIU (the PAH/PSS multilayer refractive index is determined to 1.50 by optical waveguide lightmode spectroscopy),[31] the bulk refractive index sensitivity of the bare nanorod amounts to 170 nm RIU^{-1}, in accordance with the SiO$_2$ bulk sensitivity measurements. The sensitivity of center masked and bare nanorods upon PE film deposition decreases to its $1/e$ value at a surface distance of 14 ± 1 nm and 17 ± 1 nm, respectively.

The MNPBEM based simulation plotted in Fig. 5(a) shows a faster decay of the near field in z-direction at the particle tips than the center, in agreement with the experimental sensitivity decay values. We averaged the calculated field decay lengths over the surface areas left uncovered by the masks, obtaining simulated field decay lengths for center and tip masked particles of 8 nm and 12 nm, respectively.

One might suspect that a redistribution of the plasmon mode volume caused by the masking might influence the experimental results. However, in our experience the optical near field undergoes no substantial redistribution as long as changes in the refractive index on the plasmonic particles are distributed in such a way that the symmetry of the nanostructure is maintained.[13]

Sensitivity profile in *x*- and *y*-direction

For the sensitivity characterization in *x*- and *y*-directions the effect of a small SiO$_2$ dot (20 nm diameter) attached to

selected particle sites is measured. The dielectric dots serve as models for the adhesion of large biomolecules. However, the expected wavelength shift due to the dot lies in the same range as the fluctuations in LSPR wavelength when comparing individual nominally identical nanoparticles, an effect that is caused by small lithography fabrication-related geometric variations. Therefore, we employ a row-based sample design as introduced recently.[14] In brief, the nanorods are arranged in fields of parallel rows, each row comprising 240 particles with a mutual distance of 200 nm. The distance between individual rows is chosen as 4 µm to obtain closely spaced rows that still can be probed separately by optical imaging. The nanorods of every other row are modified in a second lithography step with the SiO_2 dots (in the following we refer to these modified nanorods as "dotted"), while the nanorods in the rows in between remain bare and serve as a reference. By averaging over the spectra of all nanorods in one row the influence of the particle geometry variations on the spectral signature is sufficiently small compared to the dot-induced centroid shifts.

To improve the signal-to-noise-ratio when measuring individual nanorod rows we apply a dark field illumination setup with a tungsten white light source in a Nikon TE2000-S microscope. The illuminating light is polarized in x-direction, $i.e.$, along the direction of the SiO_2 dot displacement, $cf.$ Fig. 1(c). The scattered light of individual rows is collected with a 40×, NA = 0.75 microscope objective (Nikon, Plan Fluor), directed towards the 20 µm wide entrance slit of a photospectrometer (monochromator Andor, Shamrock SR-303i) and imaged by a camera (Andor, iXon DV885LC). For the evaluation of the LSPR spectral shift we employ again the centroid method, yielding a peak position precision of <0.1 nm. Lithographically induced deviations in geometry and thus spectral centroid position of the bare reference rows of ±0.8 nm lead to a total error of ±0.9 nm.

The lateral dot position is varied from one dotted row to the next. In four samples the SiO_2 dots are initially positioned at the nanorod center and are then stepwise moved along the x-direction up to off-center distances of 80 ± 3 nm, see Fig. 6(a). In two samples the dots are initially placed on the substrate, 40 ± 3 nm away from the nanorod center in y-direction, and are then likewise moved along the x-direction, see Fig. 6(b). The position of the dots is measured by SEM with a precision of ±3 nm, these measurements are done after the optical measurement to avoid possible particle contamination.

The LSPR shifts caused by SiO_2 dots are summarized in Fig. 7 as a function of dot position. Centroid shifts caused by dots of similar off-center positions (10 ± 5 nm, 20 ± 5 nm, $etc.$) are averaged. Fig. 7(a) and (b) show the averaged centroid shifts of four samples with the SiO_2 dot initially placed at the nanorod center and two with the dot initially placed on the substrate, with an offset of 40 ± 3 nm in y-direction, respectively. We observe the strongest redshift of the centroid wavelength when the dots are just inside the nanorod tip, in agreement with the expected (in-plane) dipolar field. Fig. 7(a) shows that the averaged redshift caused by SiO_2 dots placed at the particle tip, at off-center distances around 50 nm, amounts
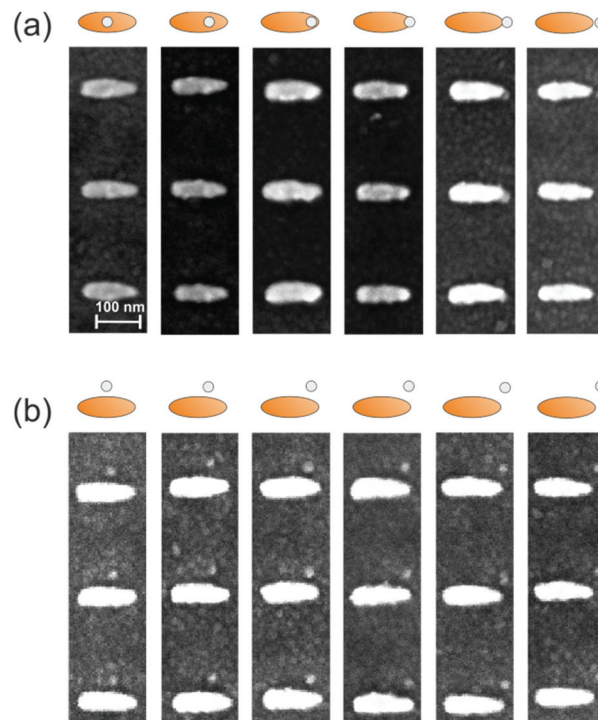
Fig. 6 SEM images showing gold nanorods and SiO_2 dots. (a) Sections of dotted rows of an exemplary sample field with dots at different positions along the long nanorod axis, together with corresponding sketches. (b) As in (a), but with a 40 nm offset in y-direction in SiO_2 dot position.

to 7.6 nm. At off-center distances below 25 nm the average redshift of the nanorod LSPR amounts to 1 nm. This implies that polymer dots positioned at the nanorod tip cause over a factor seven stronger shifts in centroid wavelength as dots near the particle center. As the dot approaches the rod tip the average redshift increases, from 3.2 nm at off-center distances around 30 nm to 6.5 nm at off-center distances around 40 nm. Going to off-center distances larger than half the nanorod length (55 nm) leads to a comparatively fast decrease in redshift until at off-center distances over 75 nm the averaged shift in centroid wavelength becomes practically zero. In Fig. 7(b), where the dot is initially placed 40 nm off the nanorod long axis, we also observe a redshift of the centroid wavelength as the SiO_2 dots approach 55 nm off-center distance, although much less distinct than in Fig. 7(a). The average redshift for off-center distances around 50 nm amounts to 4.5 nm, at off-center distances larger than the particle length the redshift rapidly tends to zero.

Numerical results of the rod's local sensitivity calculated with the MNPBEM toolbox are plotted in Fig. 7 as blue lines. The simulation reproduces well the trends and actual relative values of the experimentally observed spectral shifts for both the SiO_2 dot being placed on the particle surface and on the substrate. However, the simulated curve shows a smaller peak shift, with the discrepancy increasing close to the particle tip. We suspect that the cause for the smaller simulated shift are small topologically peculiarities originating from the litho-
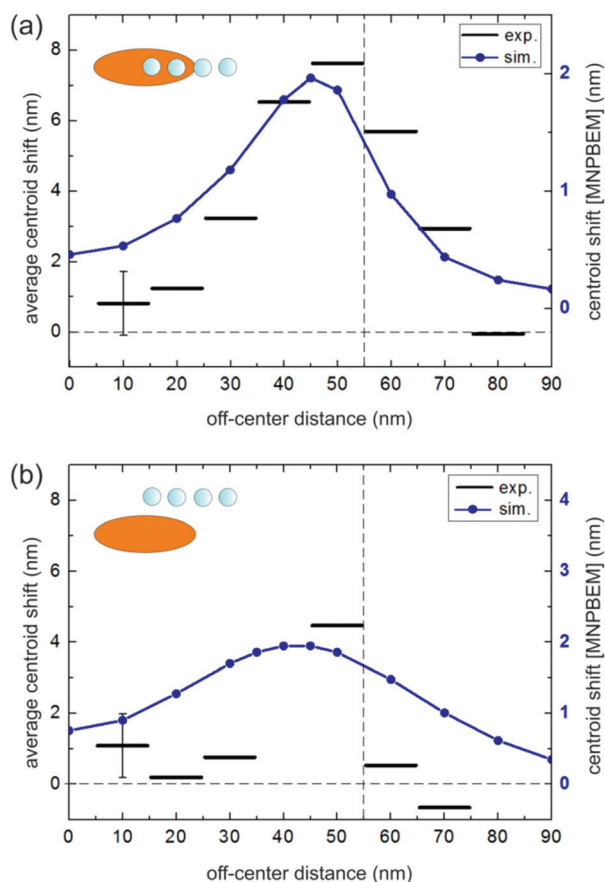
Fig. 7 Measured and simulated centroid shifts of dotted gold nanorods. The SiO$_2$ dot is initially positioned (a) at the nanorod center or (b) at a position shifted 40 ± 3 nm in *y*-direction. Experimental shift values are plotted as a function of the dot's position, the shifts of dots of similar off-center distances are averaged as indicated by the black horizontal bars. No values were measured in (b) for off-center distances around 40 nm and above 75 nm. The error is exemplarily given by the black perpendicular bars. The simulated spectral shift values are shown as blue round symbols, the blue lines are mere guides to the eye. The perpendicular dashed black lines denote the particle rim at 55 nm off-center distance. Sketches of dotted nanorods are depicted in the inset.

graphic manufacturing process the simulation can't account for, as details of the actual particle shapes on the nanometer scale are unknown.

Comparing the nanorod sensitivity with the particle field intensity in the *x*–*y*-plane (Fig. 5(b)) shows that the sensitivity curve follows the profile of the electric field, illustrating the strong correlation of electric field strength and local sensitivity. A comparison of the nanorod sensitivity at a given *x*–*y*-position to the sensitivity decay in *z*-direction further indicates that at positions of high sensitivity the particle's sensitive volume shows stronger confinement.

Especially for bio-sensing applications where low concentrations of analyte molecules are to be detected, knowledge of the position dependent dot-caused shift is substantial. Due to the limited amount of target molecules available, it is desirable for them to bind to sites of high sensitivity to cause the

maximal signal. Furthermore, quantitative results are only possible if molecules bind to sites of equal sensitivity.

Masking particles with PMMA stripes may be a quite elaborate method to restrict analyte molecule to sites of high and uniform sensitivity, but easier methods exist already. In our previous work, for example, we have shown a simple way of masking metal nanodisks to restrict analyte access to the sensitive disk rim.[14] A different approach was followed by P. Zijlstra *et al.*, who achieved selective adsorption by selectively functionalization of the tip of nanorods.[17]

Conclusions

We studied the local refractive index sensitivity of gold nanorods in three dimensions. We observe significant quantitative differences in spectral shifts depending on where we placed nm-small dielectric dots serving as model analytes. Although the experimentally obtained differences in refractive index sensitivity decay between particle tip and center were quite small, we could demonstrate in all cases clear trends to a stronger sensitivity decay at the nanorod tips both experimentally and theoretically.

Our results confirm that defining the sensitivity of nanoparticles in terms of refractive index bulk sensitivity is in most cases a too rough estimation of the particle's sensoric response. Therefore we suggest the use of a sensitivity value for locally induced spectral changes, S_{local}, that captures the particle response to changes in the refractive index of nm-small volumes V (*e.g.*, using well defined volumes as employed here for calibration). This local sensitivity definition has to give the particle sensitivity range relative to changes in the local refractive index with $S_{local\_min} = \Delta\lambda_{LSPR\_min}/(\Delta n \times V)$ and $S_{local\_max} = \Delta\lambda_{LSPR\_max}/(\Delta n \times V)$. In the case of our nanorods this would be a resonance shift of 3×10^{-4} RIU^{-1} nm^{-2} to 2×10^{-3} RIU^{-1} nm^{-2}.

The presented additional characterization of nanoparticles would not only allow a better comparison of the performance of different particles but quantitative analysis of low analyte concentrations would benefit from this clearer sensitivity definition that takes the optical properties of a specific particle plasmon sensor into account.

Acknowledgements

References

1 K. L. Kelly, E. Coronado, L. L. Zhao and G. C. Schatz, *J. Phys. Chem. B*, 2003, **107**, 668–677.
2 K. M. Mayer and J. Hafner, *Chem. Rev.*, 2011, **111**, 3828–3857.

3 E. Petryayeva and U. J. Krull, *Anal. Chim. Acta*, 2011, **706**, 8–24.

4 S. Roh, T. Chung and B. Lee, *Sensors*, 2011, **11**, 1565–1588.

5 A. G. Brolo, *Nat. Photonics*, 2012, **6**, 709–713.

6 A. B. Dahlin, N. J. Wittenberg, F. Höök and S.-H. Oh, *Proc. Soc. Photo-Opt. Instrum. Eng.*, 2013, **2**, 83–101.

7 K. Kumar, A. B. Dahlin, T. Sannomiya, S. Kaufmann, L. Isa and E. Reimhult, *Nano Lett.*, 2013, **13**, 6122–6129.

8 M. Svedendahl, S. Chen, A. Dmitriev and M. Käll, *Nano Lett.*, 2009, **9**, 4428–4433.

9 L. J. Sherry, S. H. Chang, G. C. Schatz, R. P. Van Duyne, B. J. Wiley and Y. N. Xia, *Nano Lett.*, 2005, **5**, 2034–2038.

10 W. A. Murray, B. Auguié and W. L. Barnes, *J. Phys. Chem. C*, 2009, **113**, 5120–5125.

11 J. Becker, A. Trügler, A. Jakab, U. Hohenester and C. Sönnichsen, *Plasmonics*, 2010, **5**, 161–167.

12 T. J. Antosiewicz, S. P. Apell, V. Claudio and M. Käll, *Opt. Express*, 2012, **20**, 524–533.

13 M. Piliarik, P. Kvasnička, N. Galler, J. R. Krenn and J. Homola, *Opt. Express*, 2011, **19**, 9213–9220.

14 V. Häfele, A. Trügler, U. Hohenester, A. Hohenau, A. Leitner and J. R. Krenn, *Opt. Express*, 2015, **23**, 10293–10300.

15 A. Unger, U. Rietzler, R. Berger and M. Kreiter, *Nano Lett.*, 2009, **9**, 2311–2315.

16 I. Ament, J. Prasad, A. Henkel, S. Schmachtel and C. Sönnichsen, *Nano Lett.*, 2012, **12**, 1092–1095.

17 P. Zijlstra, P. M. R. Paulo and M. Orrit, *Nat. Nanotechnol.*, 2012, **7**, 379–382.

18 T. J. Davis, D. E. Gómez and K. V. Vernon, *Phys. Rev. B: Condens. Matter*, 2009, **79**, 155423.

19 V. Claudio, A. B. Dahlin and T. J. Antosiewicz, *Phys. Chem. C*, 2014, **118**, 6980–6988.

20 U. Hohenester and A. Trügler, *Comput. Phys. Commun.*, 2012, **183**, 370–381.

21 F. J. Garcia de Abajo and A. Howie, *Phys. Rev. B: Condens. Matter*, 2002, **65**, 115418.

22 P. B. Johnson and R. W. Christy, *Phys. Rev. B: Solid State*, 1972, **6**, 4370–4379.

23 A. B. Dahlin, J. O. Tegenfeldt and F. Höök, *Anal. Chem.*, 2006, **78**, 4416–4423.

24 M. E. Stewart, C. R. Anderton, L. B. Thompson, J. Maria, S. K. Gray, J. A. Rogers and R. G. Nuzzo, *Chem. Rev.*, 2008, **108**, 494–521.

25 O. Kedem, A. Tesler, A. Vaskevich and I. Rubinstein, *Nano Lett.*, 2011, **5**, 748–760.

26 G. Decher, *Science*, 1997, **277**, 1232–1237.

27 E. Seyrek, J. Hierrezuelo, A. Sadeghpour, I. Szilagyi and M. Borkovec, *Phys. Chem. Chem. Phys.*, 2011, **13**, 12716–12719.

28 K. Kanazawa and J. G. Gordon, *Anal. Chim. Acta*, 1985, **175**, 99–105.

29 Z. Sauerbrey, *Physics*, 1959, **155**, 206–222.

30 J. J. Iturri Ramos, S. Stahl, R. P. Richter and S. E. Moya, *Macromolecules*, 2010, **43**, 9063–9070.

31 C. Picart, G. Ladam, B. Senger, J.-C. Voegel, P. Schaaf, F. G. J. Cuisinier and C. Gergely, *J. Chem. Phys.*, 2001, **115**, 1086–1094.